Observing Hurricane Harvey's Eyewall at Landfall

by Pedro L. Fernández-Cabán, A. Addison Alford, Martin J. Bell, Michael I. Biggerstaff, Gordon D. Carrie, Brian Hirth, Karen Kosiba, Brian M. Phillips, John L. Schroeder, Sean M. Waugh, C. Eric Williford, Joshua Wurman, and Forrest J. Masters

AFFILIATIONS: Fernández-Cabán and Phillips—University of Maryland, College Park, Maryland; Alford, Biggerstaff, and Carrie—School of Meteorology, University of Oklahoma, Norman, Oklahoma, Bell—WeatherFlow, Inc., Fort Collins, Colorado; Hirth and Schroeder—National Wind Institute, Texas Tech University, Lubbock, Texas; Waugh—NOAA National Severe Storms Laboratory, Norman, Oklahoma; Kosiba and Wurman—Center for Severe Weather Research, Boulder, Colorado; Williford— Weather Predict, Inc., Raleigh, NC

CORRESPONDING AUTHOR: Forrest J. Masters, Engineering School of Sustainable Infrastructure & Environment, University of Florida, 365 Weil Hall, Gainesville, FL 32611. Email: *masters@ce.ufl.edu*

> Wind velocity and radar data collected in Hurricane Harvey's eyewall at landfall offer an unprecedented glimpse into the structure of surface winds in a major hurricane.

Abstract

While Hurricane Harvey will best be remembered for record rainfall that led to widespread flooding in southeast Texas and western Louisiana, the storm also produced some of the most extreme wind speeds ever to be captured by an adaptive mesonet at landfall. This paper describes efforts by the *Digital Hurricane Consortium*, an ad-hoc group of atmospheric scientists and wind engineers to intercept and collect high resolution measurements of Harvey's inner core and eyewall as it passed over Aransas Bay into mainland Texas. The *Digital Hurricane Consortium* successfully deployed more than 25 observational assets, leading to an unprecedented view of the boundary layer and winds aloft in the eyewall. This paper presents an overview of data collection and key initial findings. Analysis of anemometric measurements and mobile radar data during heavy convection reveals the kinematic structure of the hurricane at landfall and the influence of circulations aloft on surface winds and extreme surface gusts and their relation to nearby damage. Evidence of meso-scale vortices in the interior of the eyewall is also presented. Finally, the paper reports on an atmospheric sounding in the inner eyewall that produced an exceptionally large, and potentially record value of precipitable water content for observed soundings in the continental US.

Keywords

Hurricane, Harvey, Boundary Layer, Mesoscale Vortices, Vortex Rossby Waves, Field Deployment

Manuscript

The landfall of Harvey, the first major Atlantic-basin hurricane of 2017, on the Texas coast brought to an end the record-breaking quiet period of U.S. major hurricanes dating back to Hurricane Wilma (2005). Harvey was also the first Category 4 hurricane to make landfall on the Texas coast since Hurricane Carla (1961) (Ho and Miller 1982). High oceanic heat content and favorable atmospheric conditions in the

44 western Gulf of Mexico allowed the storm to rapidly intensify into a Category 4 strength (115 knots, 938
45 mb) hurricane before it made landfall on San Jose Island on Friday evening, 25 Aug. Due to the small
46 wind footprint of the storm, the most severe winds were primarily limited to Aransas, Calhoun and
47 Matagorda counties. Heavy destruction occurred east of Corpus Christi, with smaller communities such as
48 Rockport and Fulton being strongly impacted. Harvey then drifted over Texas for five days under weak
49 steering currents. Its nearly stationary, looping motion meant that the strong rain bands east of the
50 circulation continuously tapped a rich supply of Gulf moisture across southeastern Texas and western
51 Louisiana. This setup led to record Texas and U.S. storm-event rainfall accumulations, with catastrophic
52 flooding over a wide area of southeastern Texas (NOAA NWS 2017).
53
54 This paper focuses on the first interval of Harvey's landfall, presenting a composite assessment of radar
55 and weather station observations of the storm as it moved toward and passed over Aransas Bay into
56 mainland Texas (Figure 1). Comparison of precise anemometric measurements to C-band dual-Doppler
57 data synthesis during heavy convection reveal the influence of weather structures aloft on the surface
58 wind structure, calling into question how well stationary, neutral boundary layer profiles serve as targets
59 for similitude for computational and experimental modeling of surface winds. Finally, the paper presents
60 an atmospheric sounding in the inner eyewall that appears to have produced an exceptionally large
61 precipitable water content for observed values in the continental US and one that ultimately presaged the
62 extreme rain that would flood Houston in the days that followed.
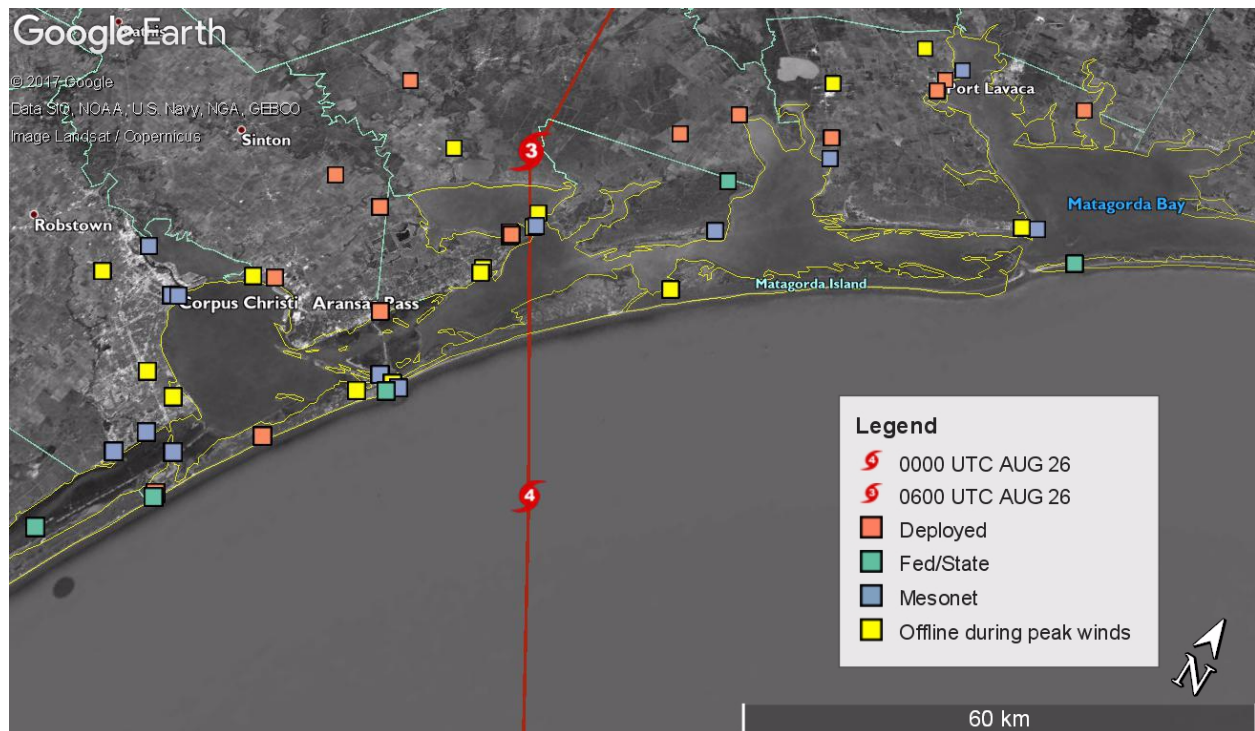63
64

65
66
67 **Figure 1.** Map of all in situ and adaptive surface assets deployed for hurricane Harvey, with the stations
68 denoted in yellow indicating the stations that did not capture peak winds due, for example, to station
69 failure/destruction, loss of power, loss of connectivity, or loss of data. The dataset was significantly
70 enriched by the deployed and private mesonet assets, most notably in the swath of very high impact from
71 Holiday Beach, through Rockport, to Port Aransas. The more specialized adaptive and local mesonet
72 observations proved to be collectively more reliable than the in-situ state and federal networks, yielding a
73 75% success rate in capturing peak winds verses a 36% for the state and federal sites.

74

OBSERVING SYSTEMS

76
Data were collected by members of the Digital Hurricane Consortium (Figure 2), which is an ad-hoc
group of engineers and scientists that deploy weather stations and mobile Doppler radars in the hurricane
landfall region to study a diverse range of topics such as wind speed conversion (e.g., Kosiba et al., 2015;
Masters et al. 2010), boundary layer variability (Wurman and Winslow 1998; Knupp et al. 2006; Lorsolo
et al. 2008; Hirth et al. 2012), electrification (Pilkey et al. 2013), inner core dynamics (Alford and
Biggerstaff 2015; Alford et al. 2016), and eyewall asymmetries and mesovortices (Wingo and Knupp
2016). The program collects perishable meteorological data in the landfall region leading up to and
through landfall. In addition to basic research, these measurements are used by the operational
meteorology, emergency management, and catastrophe modeling communities to monitor decaying
weather conditions at landfall and to analyze the surface wind field post-event. For the members of this
program, which have collected surface observations in landfalling storms since the late 1990s, Harvey is
most intense storm captured to date.
89

	Center for Severe Weather Research (CSWR). The Doppler on Wheels (DOW) radar network is part of the National Science Foundation Lower Atmospheric Observing Facilities. CSWR fielded one DOW radar (DOW8) and four ruggedized 1-m AGL weather stations ("Pods") during Harvey. DOW8 was configured as a single-beam single-pol X-band system, operating at 9.45 GHz. DOW8 employs a 250 kW transmitter and the 2.44-meter antenna resulting in a 0.9-degree beamwidth, indexed at 0.5 degrees. During Hurricane Harvey, the pulse width (gating) initially was 0.167 us (12.5 m) and then increased to 0.333 us (50 m) during the eye. A ¾ staggered pulse repetition time was used, resulting in an effective Nyquist velocity of 95 m s^{-1} (0.167 μs pulse) and 71 m s^{-1} (0.333 μs pulse). DOW8 did full surveillance scans completing 360 degrees in 9-12 seconds, depending on wind conditions. The DOW8 mast housed a RM Young anemometer (5103), with 1 Hz observations at 8 m AGL. More information about CSWR instrumentation can be found at *cswr.org*.
	Florida Coastal Monitoring Program (FCMP). The FMCP deployed two ruggedized weather stations equipped with precision ultrasonic anemometers (WindMaster Pro Model 1561-PK-020) installed at 5, 7.5, 10, 12.5, and 15 m above ground level. The units have a wind speed range of 0–65 m/s with a resolution of 0.01 m s^{-1}, and measure instantaneous three-dimensional wind components with a maximum sampling rate of 32 Hz. A National Instruments Compact-RIO system digitally polled the anemometers at 10 Hz to synchronize data acquisition and eliminate jitter. More information about the FCMP infrastructure may be found in Balderrama et al. (2011) and *fcmp.ce.ufl.edu*.

	NOAA National Severe Storms Laboratory (NSSL). NSSL deployed a Mobile Mesonet/Mobile Sounding vehicle which is capable of taking surface measurements of temperature, pressure, wind speed/direction, relative humidity, and solar radiation as well as being able to launch soundings. The surface winds are measured at 3.35 m using an RM Young 05103 Wind Monitor which has a range of 0-100 m s^{-1} with a resolution of 0.3 m s^{-1}, sampled at 1 Hz. A Vaisala MW41 sounding system is used to collect sounding data with either an RS92-SGP or RS41 radiosonde. More information can be found at nssl.noaa.gov/tools/observation.
	Texas Tech University (TTU). TTU deployed 14 StickNet (Weiss and Schroeder, 2008) weather monitoring stations to the landfall region to provide research grade measurements of wind speed, wind direction, pressure, temperature and relative humidity. Near surface wind measurements were acquired at a height of 2.25 m AGL using a RM Young 05103 Wind Monitor and a sample rate of 10 Hz. Summary information, including compass corrected wind directions, was relayed every minute via a cell network connection. All deployments were made in the coastal counties in open or marine exposure.
	University of Oklahoma (OU). OU deployed the SR2 C-band Shared Mobile Atmospheric Research and Teaching (SMART) radar (Biggerstaff et al. 2005; 2017). SR2 operates at 5540 MHz with 300 kW of power split down the two waveguide channels for simultaneous transmit/receive dual-polarization. The 2.54 m reflector provides a beamwidth of 1.5°. The radar initially operated on a 12-minute schedule with 3 eastern sector volume scans, each taking 3 minutes to complete, followed by a surveillance scan and a user-specified range-height indicator (RHI) scan. As the eyewall came ashore, the sector scans were replaced with 2 full volume scans and the RHI scans were eliminated. SR2 was approximately synced with the Corpus Christi WSR-88D for dual-Doppler wind retrievals over the inner core and eyewall region of Harvey.

Figure 2. Observational assets in the Digital Hurricane Consortium

A network of 14 federal and state surface observations stations also reside in the landfall region. These are supplemented by 19 local mesonet stations from WeatherFlow, TCOON and Earth Networks. These stations collect a range of surface wind data, from the 15-minute averages of the NOS/NERRS sites, to the 3-second data from the Hurricane Hardened WeatherFlow network. The appendix contains metadata (e.g., height, sampling characteristics) for the non-federal mesonets.

THE INTERCEPT

TTU sent a team from Lubbock to Corpus Christi on Wednesday, 23 August, to scout for potential deployment sites with the goal of creating a measurement array on each side of the anticipated landfall

103 point, while ensuring these sites provided reasonable access and sufficient elevation to protect from storm
104 surge and freshwater flooding. Potential access difficulties forced the team to reposition to Mustang
105 Island early on 24 August, where deployment of StickNets was initiated. Research personnel then
106 deployed three additional stations near the more densely populated areas of Portland, Aransas Pass and
107 Copano Village, followed by a move northward into rural areas near Port Lavaca to complete a total of
108 eight deployments for the day. The next morning on 25 August, TTU added three stations to extend the
109 network northward and protect against any northward drift of the landfall point. As uncertainty in the
110 track guidance dropped during the day, the team circled back south to densify the mesonet near Fulton,
111 which is located to the east of Rockport and to the west of Aransas Bay.
112
113 On 24 August, the OU/NSSL teams deployed four researchers in three vehicles carrying mobile radar,
114 anemometers, and upper air measurement equipment, reaching the Texas coast on the morning of 25
115 August. The C-Band SMART radar was eventually deployed near Woodsboro, TX along US 77 to sample
116 the eyewall and inner core structure of the hurricane during landfall without putting the team in the direct
117 path or at risk of flooding (Fig. 3). Radar operations started at 2002 UTC on 25 August and concluded at
118 1430 UTC on 26 August. There were two periods during which the radar was down due to loss of antenna
119 control caused by strong gusty winds during RHI scans: from 2310-2349 UTC and 0145-0312 UTC. In
120 all, more than 16 hours of dual-Doppler coverage with the Corpus Christi WSR-88D was obtained during
121 the hurricane's landfall. As Harvey approached and made landfall late Friday evening, the NSSL Mobile
122 Mesonet launched two radiosonde soundings near Woodsboro into the outer rainbands (1954 UTC on the
123 25th and 0136 UTC on the 26th) and performed several transects through Harvey's western precipitation
124 region as conditions permitted. The eyewall convection was strongest on the western quadrant of Harvey
125 and remained so during landfall. At approximately 0430 UTC 26th Aug, a brief transect was made into
126 the outer edge of the western eyewall along US 188 east of Sinton, TX. At approximately 0600 UTC 26th
127 Aug, it was determined that conditions permitted the redeployment of the mobile mesonet to a location
128 within Refugio, TX to facilitate both direct surface observations of the eye and eyewall as it passed over
129 and to launch a sounding within the eye itself. At 0716 UTC, the third and final sounding of the
130 deployment was launched in Refugio, TX. The mobile mesonet collected 1 second surface observations
131 from a period spanning roughly 1830 UTC on Aug 25th to 1630 UTC on Aug 26th.
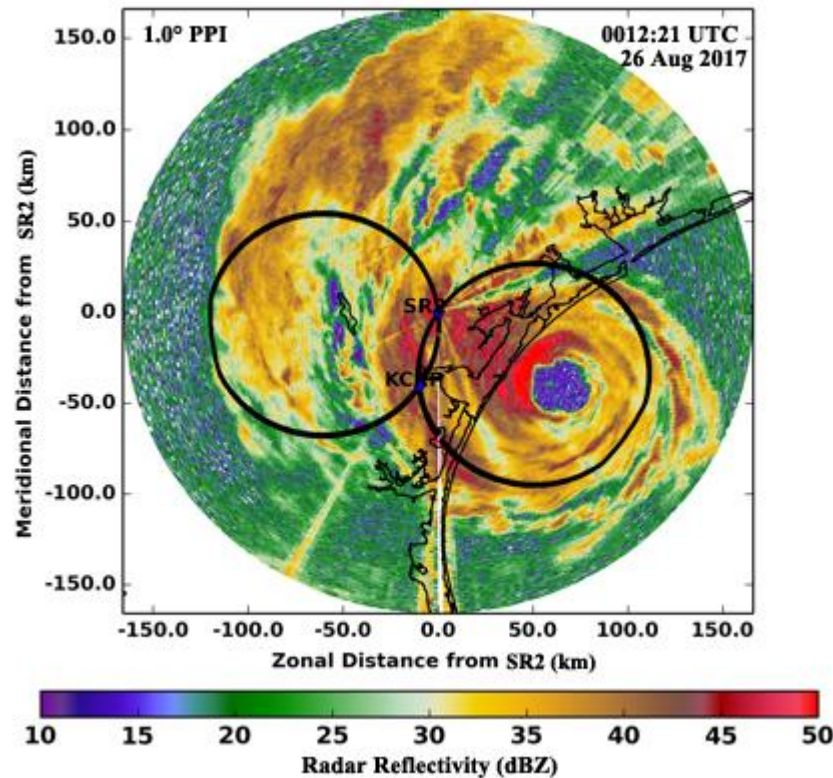
Figure 3. Radar reflectivity at 1.0 degree elevation angle from SR2 radar at 0012 UTC on 26 August 2017 showing the location of Harvey's eye relative to the dual-Doppler lobes (black circles) in which the three-dimensional flow can be retrieved.

The FCMP team (led by the University of Florida and the University of Maryland) mobilized two 15 m weather stations (T2, T3) late Thursday afternoon (24 August), sending 11 research personnel and four chase vehicles. Following the 10 CDT NHC forecast and with consultation with WeatherPredict, Inc., the FCMP team arrived in Port Lavaca on 25 August to initiate deployment of weather station T2 in suburban conditions to study the wind structure of the roughness sublayer. Forecast guidance subsequently shifted the landfall forward approximately six hours, forcing the team to split into two to complete the deployment. After consulting with local authorities and reviewing storm surge and wave (ADCIRC/SWAN) predictions from the Coastal Emergency Risks Assessment tool, the first team deployed T3 in the parking lot of a store located in a suburban neighborhood 500 m from Lavaca Bay. The second FCMP team drove to Fulton where CSWR had recently arrived to deploy the X-band DOW8 radar and multiple weather stations. Coordinating with the Aransas County Airport manager, both teams deployed on site in the afternoon. The FCMP deployed T3 at the western edge of the runway, which presented nominally 500-1500 m of open exposure (i.e., smooth, flat terrain) in the expected prevailing wind direction. The weather stations collected data continuously through landfall, capturing five levels of 3D ultrasonic wind data at the T2 and T3 sites, respectively.

CSWR advance teams scouted locations for DOW8 and Pods along the coastline from Corpus Christi to Long Mott, settling on the Aransas Airport as the closest well exposed, low-horizon site to the anticipated landfall point. CSWR deployed DOW8 and two Pods on a taxiway at the airport, and two additional Pods on the bridge across the inlet between Copano and Aransas bays a few kilometers to the north. DOW8 raised a masted anemometer to a height of 8 m AGL. The DOW8 radar collected data from 2220 UTC (25 August) to 0203 UTC (26 August) and then again from inside the eye from 0356 to 0540 UTC (26

160 August). The DOW8 anemometer collected data from the start of the deployment at ~2200 UTC (25
161 August) until ~0700 UTC (26 August) and the Pods collected data from the start of the deployment until
162 they were hit by debris, which varied by Pod from ~0130 - 0230 UTC (26 August).
163

164 **DOPPLER RADAR ANALYSIS**
165

166 As noted in the National Hurricane Center Tropical Cyclone Report for Hurricane Harvey (Blake and
167 Zelinsky, 2018), mesovortices were observed during landfall. Dual-Doppler analysis (Fig. 4) shows
168 several inner core rainbands that likely developed in associated with vortex Rossby waves (Abdullah
169 1966; Montgomery and Kallenbach 1997; Chen and Yau 2001; Corbosiero et al. 2006; Menelaou and
170 Yau 2014; Gao and Zhu 2016) that were emanating from asymmetries in the eyewall convection,
171 numerous rapidly developing outer rainbands, the eyewall itself, and a handful of mesocyclone-scale
172 vortices that circulated along the interior of the eyewall. These features (Fig. 4a, b) propagated
173 azimuthally along the radial gradient in vorticity (Fig. 4c) and appeared to lead to the formation of
174 sheared vortex Rossby waves radially outward from the eyewall. The waves in the interior of the eyewall
175 were associated with regions of strong radial inflow and outflow (Fig. 4b), suggesting the waves
176 redistributed momentum in the eyewall region.
177

178 The transport of high entropy air from the eye into the eyewall is thought to enhance local convective
179 instability (Braun 2002; Persing and Montgomery 2003; Eastin et al. 2005). Indeed, similar to the
180 mesovortex observed over water in Hurricane Hugo (Black and Marks 1991; Marks et al. 2008), the
181 mesovortex observed in Harvey at 0314 UTC was near the inner edge of a strong reflectivity core in the
182 eyewall convection. However, the mesovortex in Harvey also formed near the land-ocean interface where
183 enhanced low-level convergence from the change in surface roughness (c.f. Hirth et al. 2012) would have
184 further enhanced low-level vorticity. It is possible that the vortex Rossby wave generated by the
185 convective asymmetry in the eyewall of Harvey produced a vorticity perturbation that was stretched by a
186 low-level updraft fed by the boundary-layer convergence along the land-ocean interface. A similar
187 evolution was observed during the landfall of Hurricane Hermine in 2016 (Alford and Biggerstaff 2017).
188 In Hermine, low-level convergence along the ocean-land interface led to the development of a cyclonic
189 eddy along the inner edge of the eyewall and a 20 percent increase in the wind speed. The Harvey
190 mesovortex was also associated with a reflectivity filament that extended inward towards the center of
191 circulation. Aberson et al. (2006) noted a similar reflectivity feature for a mesovortex found along the
192 inner edge of the eyewall of Hurricane Isabel.
193

194 Over water, extreme gusts and strong vertical drafts have been previously documented in
195 meso/misovortices in the vicinity of hurricane eyewalls (Marks et al. 2008; Aberson et al. 2017).
196 Mesovortices near the land-sea interface, like the one observed in Harvey, have been documented
197 previously in Tropical Cyclone Oliva by Black et al. (1999). In Olivia, a mesovortex produced several
198 three second gusts in excess of 102 m s^{-1} on the interior edge of the eyewall with gust factors that exceed
199 2.5 times the background flow. Unfortunately, comparison between radar derived wind fields,
200 precipitation structure, and ground-based in situ observations was not possible for Oliva.
201

0314 UTC | z = 0.50 km MSL | Harvey

(a) Z_H and Tangential Wind Vectors (m s^{-1})

(b) Z_H and Radial Wind Vectors (m s^{-1})

Z_H

(c) | V_H | (every 5 m s^{-1}) and ζ (colors; s^{-1})

V_{Max} = 77 m s^{-1}

Vort (x10^{-3} s^{-1})

(d) KCRP Dealiased V_R - 031302 UTC - 0.5°
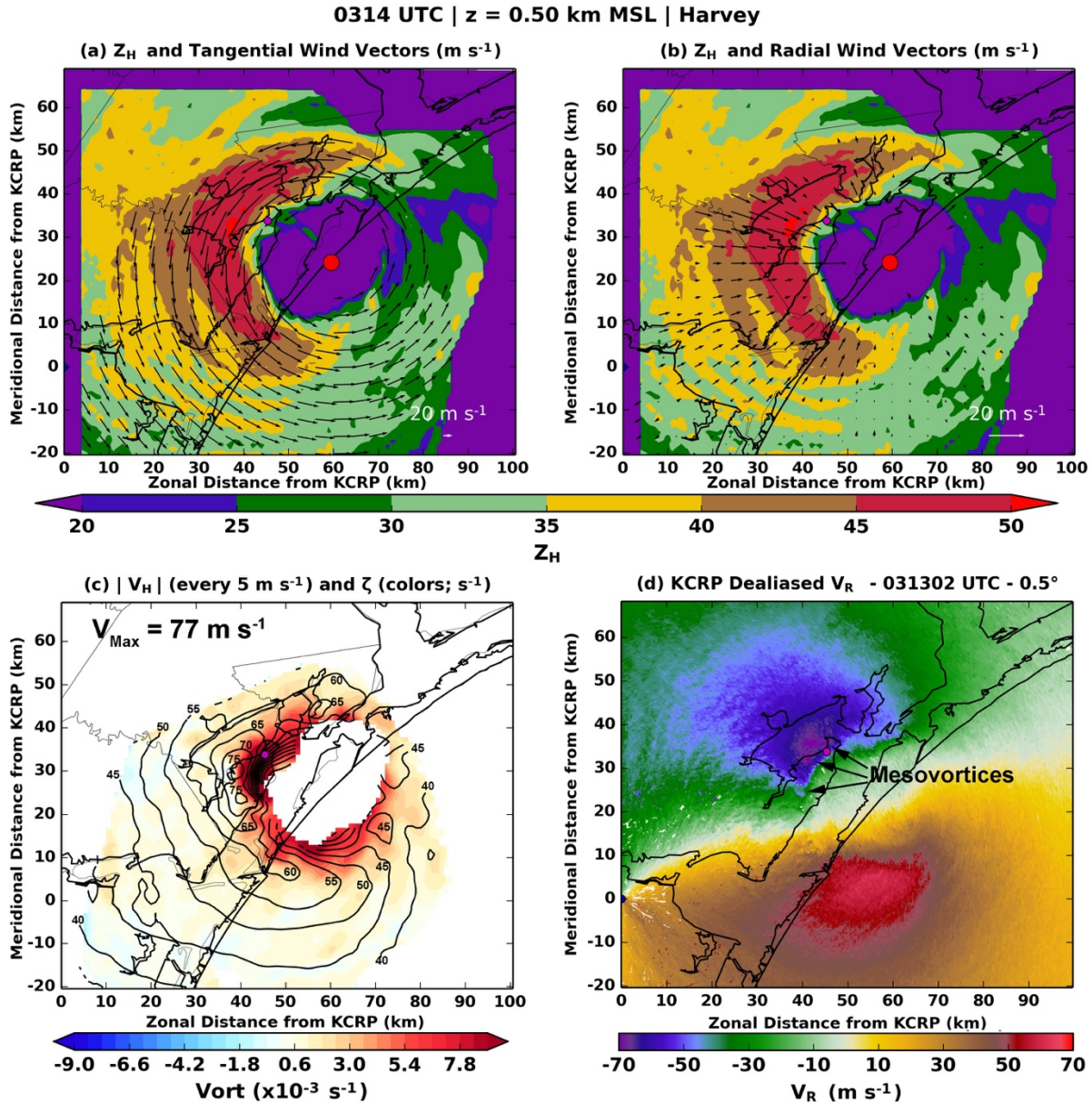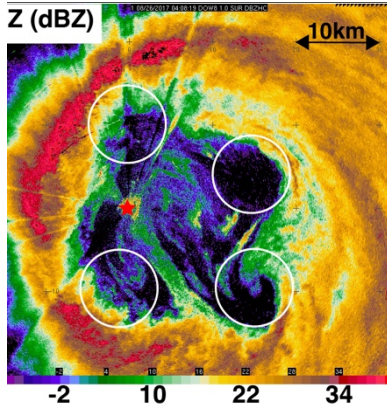
Mesovortices

V_R (m s^{-1})

Figure 4. Dual Doppler analysis of the OU SMART Radar (SR2) and KCPR WSR-88D at 0314 UTC showing (a) the tangential component of the wind overlaid on radar reflectivity, (b) the radial component of the wind overlaid on radar reflectivity, and (c) wind speed contours overlaid on vertical vorticity. The 0313 UTC KCRP WSR-88D dealiased radial velocity at 0.5° elevation angle is shown in (d). Note the different scales for the 20 m s^{-1} wind speed in panels (a) and (b). The large red dot in (a) and (b) indicates the estimated location of the center of the eye. The smaller purple dot in all panels is the location of the T2 tower deployed by the FCMP.

Additional mesovortices in Harvey were observed by CSWR DOW8 before and after the eyewall passed their location. Prior to passage of the eye, DOW8 conducted shallow volumes scans (0.5, 1.0, 1.5 degree elevation) with short gates (12.5m) and reduced range (12.5 km) to capture the evolution of coherent boundary layer structures, such as hurricane boundary layer streaks and rolls (e.g., Wurman and Winslow 1998; Morrison et al. 2005; Lorsolo et al. 2008; Kosiba et al. 2013). The DOW collected ~four hours of

7

217 data in this mode before the antenna failed due to the high winds. By 0356 UTC, once DOW8 was in the
218 eye, the winds at the DOW8 location had subsided and scanning resumed. DOW8 conducted fast
219 surveillance scans at ~1 degree elevation, with 50 m gates and 50 km range, from inside the eye of
220 Harvey (Fig. 5).
221
222 The range of the mesovortices from the 0.9-degree beamwidth DOW varied from less than 5 to ~20
223 kilometers, allowing for the fine temporal-scale observation and tracking of several eyewall mesovortices
224 (5- 8 km in diameter) (Fig. 5). Additionally, tornado-scale vortices (TSVs), with diameters of ~1 km,
225 were observed in the eyewall (Fig. 5c). These TSVs were associated with some of the most intense near-
226 surface Doppler velocities and correlated with regions of enhanced damage (Wurman and Kosiba, 2017).
227

(a) Radar reflectivity of eyewall mesovortices (white circles) at 0408:18 UTC
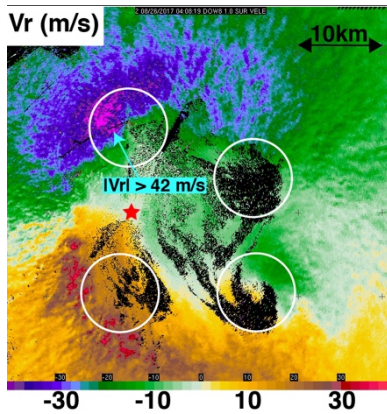
(b) Corresponding Doppler velocity. Magenta velocity contours depict Doppler winds in excess of 42 m s^{-1}.
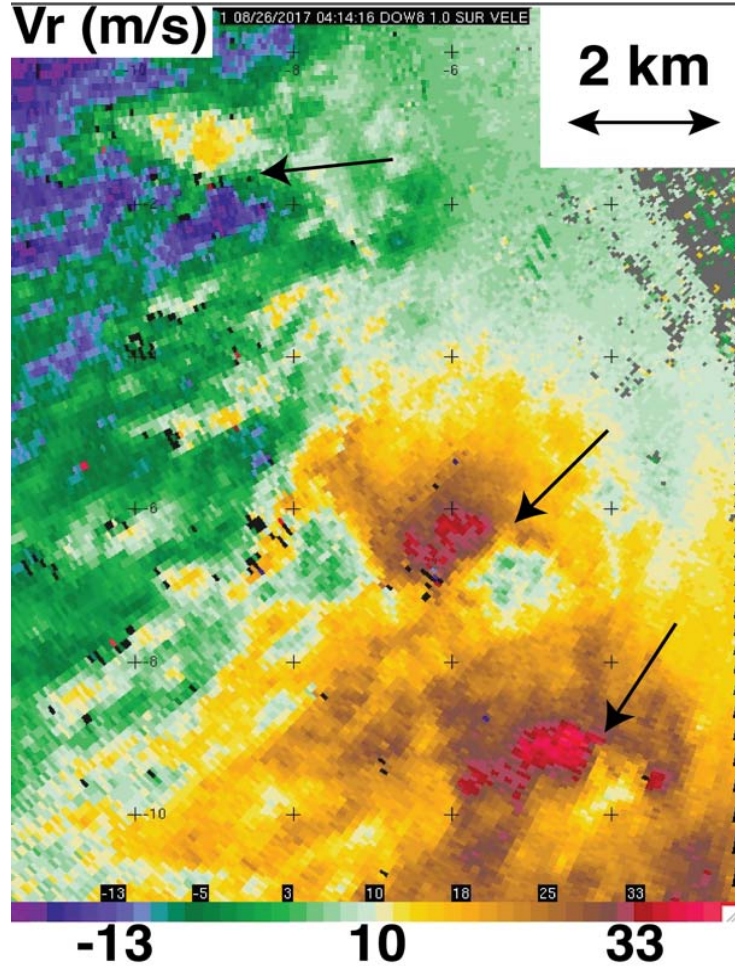
(c) Tornado-scale vortices (TSVs) observed by DOW8 at 0414:16. Arrows indicate the location of three prominent TSVs. Shown is Doppler velocity in m s^{-1}.

228
229 **Figure 5.** Radar observations by the DOW8 mobile radar (red star)
230

231

THE SURFACE WIND FIELD

By most measures, the event was extreme. Consider that the main wind loading provisioning guidance in the US (ASCE 7; 2016) bounds the design wind speed for the Texas coastal region between Corpus Christi and Houston by 63- 67 m s^{-1} isotachs referenced to a 3 s gust at 10 m in open exposure terrain. These gust speeds correspond to a 700 year mean recurrence interval, i.e., a 1/700 likelihood these wind speeds will be exceeded in a given year. Figure 6 presents the sustained and peak gust wind speed measurements for the adaptive and fixed observational networks. It is evident from the magnitudes shown that the highest wind speeds were confined to approximately 30 km on either side of the track.

241
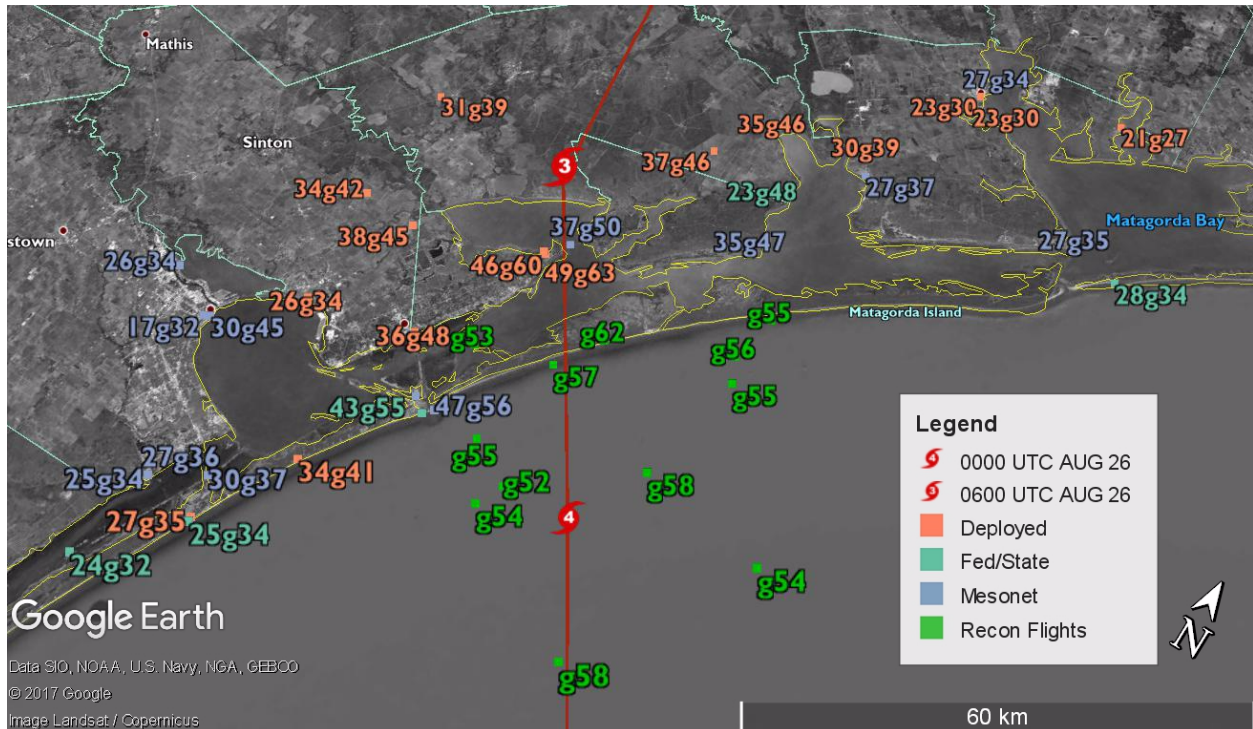
Figure 6. Storm maximum sustained wind speeds and gusts (m s^{-1}) for all fixed, portable and mobile observing platforms that captured peak winds at some point during Harvey's landfall. The USAF reconnaissance flight data are the maximums observed in the eyewall during SFMR transects, and the lowest 150 m averages of the eyewall dropsondes. Data in this figure represent a variety of observational techniques and averaging times which are detailed in the appendix.

The highest wind speed observations in the storm obtained by the Digital Hurricane Consortium were measured in the Fulton and Rockport areas, where extreme damage was observed. Figure 7 shows photos that were taken approximately 300 m north of DOW8 and FCMP T2. A garage was destroyed and at least two vehicles inside were lofted into the building.

254

9

Figure 7. Damage to a building and lofted cars near the DOW8 location at the Aransas County Airport potentially associated with the passage of a TSV. Top shows the south face of the building and bottom shows the north face of the building. Yellow rectangles outline lofted cars and red arrows indicate nearby cars that were not lofted.

Figure 8 shows the measured wind speeds from four observations collected by the FCMP and CSWR assets at the site, which were located 500 m apart. Three second gust speeds were on the order of 60-63 m s^{-1} at the 15 m elevation in open exposure conditions, which implies that coastal portions of Calhoun and Matagorda counties most likely experienced what structural engineers would term a design level event under the modern wind load provisioning standard. The peak instantaneous (0.1 s) wind speed measurement was measured by a Gill WindMasterPro ultrasonic 3-axis anemometer located at 15 m AGL on the FCMP T2 weather station. Surprisingly, the instrument—which has a published rating of 0-65 m s^{-1} (0-145 mph)—measured values ranging from 78-86 m s^{-1} (174-191 mph). Results from additional testing was performed by the manufacturer to quantify the data dropout rate suggest these data cannot be ruled out as viable observations.
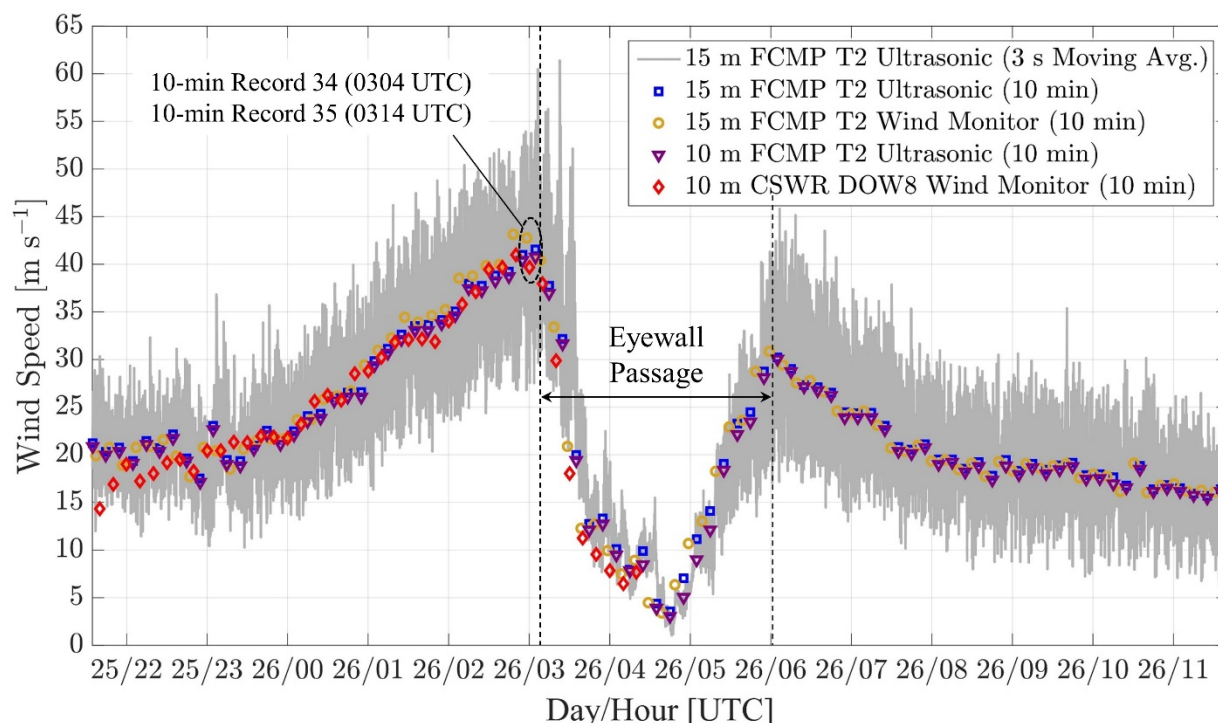
Figure 8. Anemometric records obtained at the Aransas County Airport, in Fulton, TX. Color markers correspond to 10-min non-overlapping (block averaged) mean wind speeds obtained from FCMP T2 anemometers and CRWR DOW8 wind monitor. The 3 s moving average wind speed trace for the 15 m ultrasonic anemometer is depicted in gray.

The location of the weather stations under the dual-Doppler lobes of the ground-based radars provided a rare opportunity to study the effect of the mesovortices aloft on the surface wind field. Figure 9 shows the two ten-minute non-overlapping records containing the largest observed gusts in Hurricane Harvey and their associated wind direction. Gust factors, i.e. the ratio of the short duration peak to the mean of its record, for the two 10 min records are depicted in Figure 10. The records, which were obtained during the same interval as Figure 4, immediately precede the passage of the eyewall.
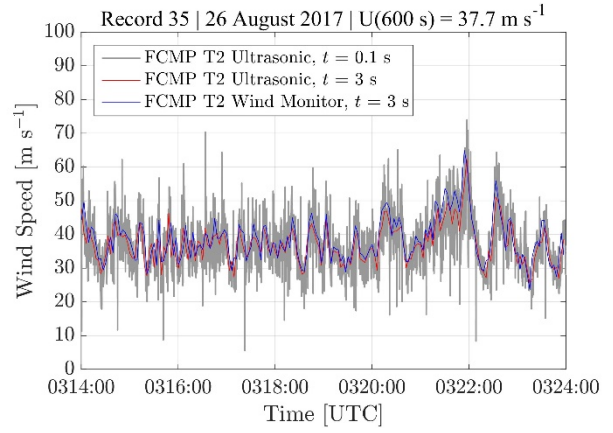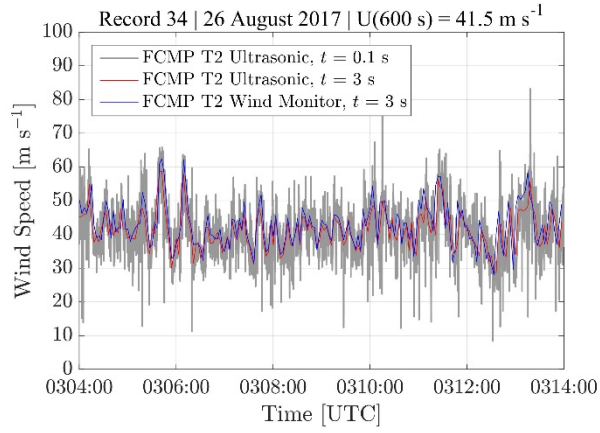
Figure 9. Ten-minute records of wind speed and direction collected by FCMP tower T2 starting at 0304:00 (a) and 0314:00 (b) UTC. The red and blue wind traces are 3 s segmented (block) averages, while the gray velocity traces correspond to instantaneous (10 Hz) records from the ultrasonic anemometer. The wind monitor and ultrasonic anemometer were located 15 m AGL.

Record 34 | 26 August 2017 | U(600 s) = 41.3 m s^{-1}

Record 35 | 26 August 2017 | U(600 s) = 37.3 m s^{-1}

(a)

(b)

Figure 10. Gust factor analysis of 10-min wind records obtained from FCMP tower T2 at 0304 UTC (a) and 0314 UTC (b). The two records show significant deviations of measured gust factor values from the theoretical model at lower gust durations.

Around 0314 UTC, the radar-retrieved wind speed at 500 m over T2 was 57 m s^{-1}. The tower was located in a region of strong cyclonic shear that was slightly upwind of the strongest winds that exceeded 80 m s^{-1} at 500 m altitude. The cyclonic shear was evident in both the tange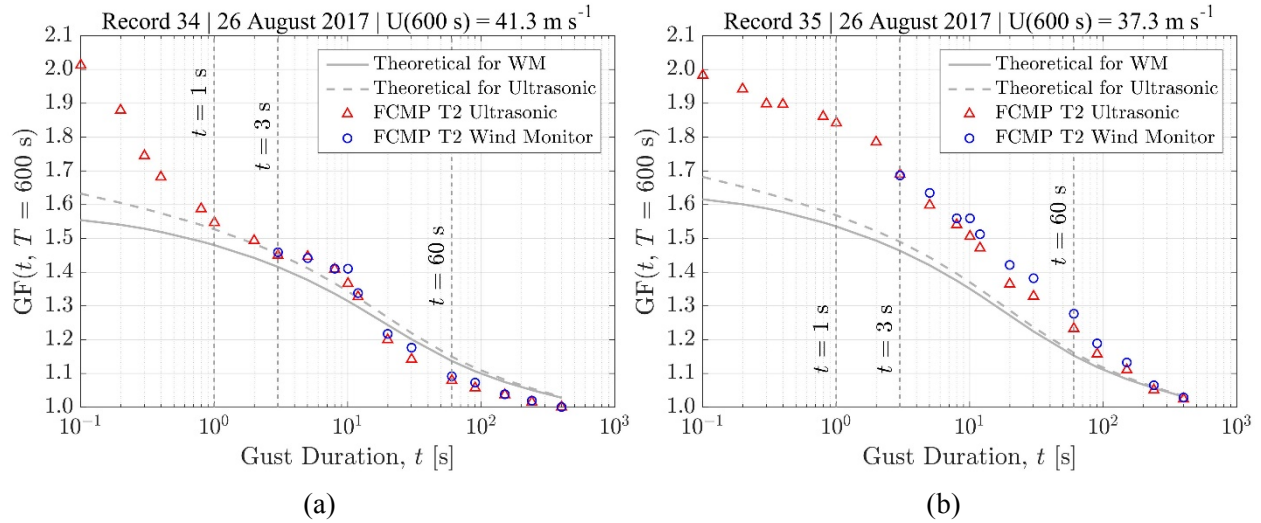ntial winds along the inner edge of the eyewall (Fig. 4a) as well as azimuthal gradients in the radial wind (Fig. 4b). A reflectivity filament attached to the strongest shear zone and extending into the eye of Harvey was also evident near T2. Within two minutes, the asymmetries were associated with mesocyclones (Fig. 4d), one of which passed close to T2.

While it is difficult to pinpoint the exact time the mesovortices passed over the site due to the temporal resolution of the radar data, pronounced variations in the flow are observed in the surface wind field record at multiple timeframes: 0305, 0311 and 0322 UTC. While pronounced variations in the flow are common in tropical cyclone measurements, these data are noteworthy in the context of quantifying the behavior of extreme winds. The dominant assumption in wind engineering is that velocity records can be considered as weakly stationary, and thus they can be described by an established power spectral density model such as the form of von Kármán (1948). These features, which lasts up to two minutes and span kilometers in scale, simply are not expected to be captured by spectra models calibrated to grid turbulence or mechanical turbulence generated by rough terrain.

Further, the effect is seen clearly in Figure 10, which compares observed gust factors (GF) to theoretical models derived from grid turbulence. The blue markers show the Wind Monitoring measurements. In the first record (Fig. 10a), the theoretical gust factor matches the observations until t = 1 s. The accuracy of measured GF at low gust durations might be limited by the sampling resolution of the sensors—e.g., the gust factor for t = 1 s was computed from the average of 10 data points (i.e., 10 Hz x 1 s). However there is a clear mismatch over the entire range of gust durations for record 35 (Fig. 10b) caused by the non-stationary event that begins at approximately 0321 UTC (Fig. 9b). A rapid change in wind direction— approximately 25 degrees—is observed during this non-stationary event (lower panel of Fig. 9b). Inspection of higher order statistical moments of the wind velocity time histories in Fig. 9b revealed strong non-Gaussian flow behavior. The 15-m ultrasonic velocity trace exhibited skewness and kurtosis values of 0.87 and 4.13, respectively. However, positively skewed distributions were also detected in the 10 min segment stating at 0304 UTC (Fig. 9a), where values of 0.27 and 3.69 were obtained for skewness and kurtosis, respectively. Collectively, the observations point to the need to incorporate non-stationary

13

347 gust loading models (e.g., Kwon and Kareem, 2009; Fernández-Cabán and Masters, 2017) and to advance
348 the utilization of computational fluid dynamics models (e.g., large eddy simulation) coupled with
349 numerical weather prediction tools.

PRECIPITABLE WATER CONTENT

351
352 A unique aspect of the deployment to Hurricane Harvey was the ability to obtain a vertical sounding from
353 inside the closed eye structure. Though not the first sounding of its kind (e.g., Franklin et al., 1988),
354 surface-based soundings in hurricanes, specifically in the eye or eyewall of hurricanes, are a rare
355 occurrence. McCaul (1991) stated that RAOB data inside the core regions of hurricanes is lacking, and
356 would be useful in characterizing the environment of landfalling systems. Given the spacing of the RAOB
357 network and the difficulty of launching soundings in hurricane conditions, McCaul (1991) further argued
358 that mobile *in situ* crews would be a potential source of these soundings. Understanding the inner core
359 environment of landfalling hurricanes is paramount to issues such as tornadoes during landfall of tropical
360 cyclones (Curtis 2003; Baker et al. 2008). While dropsondes are regularly utilized by NOAA to facilitate
361 measurements of the vertical profile of hurricanes and their environment, such observations are collected
362 mostly over the open ocean and none within the eyewall of a landfalling hurricane. Moreover, the slow
363 ascent rate (nominally 5 m s^{-1}) of a balloonborne upsonde provides much finer detail of the vertical
364 structure of land falling hurricanes and their environment than the ~11-21 m s^{-1} descent speeds of
365 dropsondes. Given the need for observational data at a high temporal frequency and at small ranges from
366 the hurricane center, a mobile sounding vehicle was used to obtain several vertical profiles throughout the
367 course of the landfall of Hurricane Harvey.

368
369 After positioning in Refugio, TX ahead of the approaching eye, a sounding was launched at 0716 UTC on
370 26 August on the inner eyewall boundary to the calm eye center (Fig. 11). The balloon rose with an
371 average velocity of ~2 m s^{-1} and proceeded to follow the inner eyewall boundary as it traversed the entire
372 circumference of the eye, passing directly over the launch point roughly 50 mins later at an altitude of
373 roughly 7.5 km. Due to the structure of the winds around the hurricane circulation, the hodograph was
374 plotted as a nearly complete circle, making 1.25 rotations around the eye wall before the balloon burst at
375 an altitude of 9.6 km and 307 mb. The observed hodograph lead to storm relative helicity (SRH) values of
376 -1847 m^2 s^{-2} in the 0-3 km layer and -758 m^2 s^{-2} in the 0-1 km layer, while the thermodynamic profile
377 showed saturated conditions for the entire flight. For context, values of 300-400 m^2 s^{-2} 0-3 km SRH
378 represent typically significant severe weather days in the central plains of the United States.

379
380 Precipitable water is defined as a measure of the depth of liquid water at the surface that would result if
381 all water vapor was precipitated out in a column. As a more practical use, the value is used to gauge the
382 moisture content of the atmosphere and asses a flooding risk. With the saturated conditions and low
383 surface pressure, the precipitable water content was measured at 8.28 cm for the Hurricane Harvey
384 sounding at 0716 UTC. To place this value into context, it is likely the highest precipitable water value
385 observed from a standard radiosonde flight without data errors in the CONUS according to the sounding
386 climatology archive maintained by the Storm Prediction Center (Rogers et al., 2014). Strictly speaking
387 there are a number of soundings in the archive with values higher than 8.28 cm, but these soundings are
388 either incomplete or contain obvious errors which lead to artificially inflated precipitable water values.
389 The climatology of soundings can be used to delineate a risk of heavy rain, with observed values above
390 the 75th percentile being an indication of a strong possibility of very heavy rain. Generally, values above
391 5.08 cm suggest excessive rainfall and flooding may be a concern (personal communication, Jonathan
392 Kurtz, Senior Forecaster NWS). .
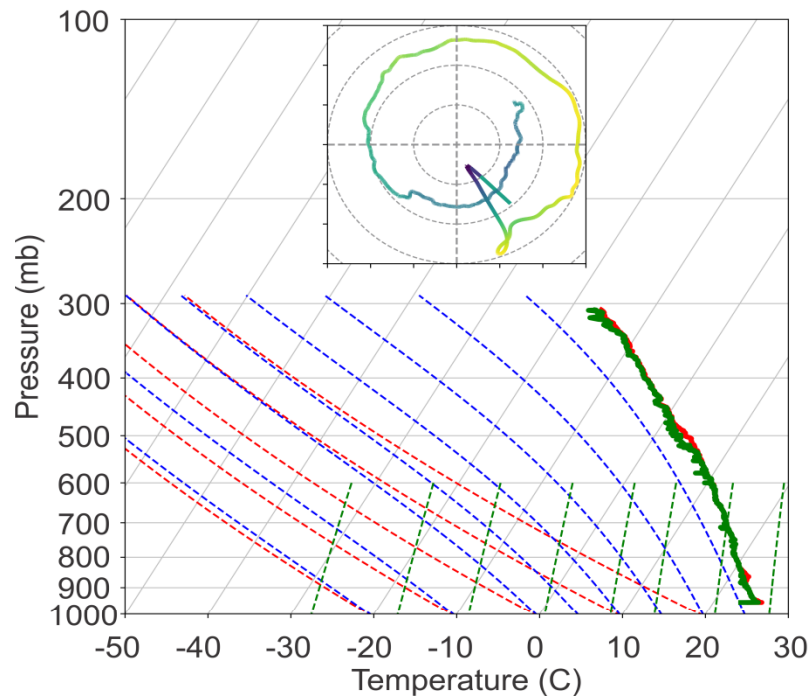
Figure 11. Sounding in the inner eyewall from a launch at 0716 UTC near Refugio, TX on 26 August 2018 obtained by NSSL and OU. The circular hodograph represents 0-3 km storm relative helicity value of -1847 m^2 s^{-2}, and the total profile contains 8.3 cm of precipitable water.

This sounding, and others obtained in Hurricane Harvey, demonstrate the extreme environment present in landfalling tropical systems. Furthermore, rapid changes in this environment occur when approaching the center of circulation. More observations of this environment, and the changes it undergoes as the system transitions to extratropical, are need to fully understand the landfalling process and the associated risks it presents.

FINAL REMARKS

Extreme winds with gusts over 60 m s^{-1} were found along the inner edge of the eyewall of Hurricane Harvey during landfall. Based on dual-Doppler wind retrievals from a SMART radar and the NWS WSR-88D in Corpus Christi, TX, these winds appear to be associated with the passage of a mesovortex observed along the inner edge of the eyewall of Harvey. The finer-scale structure of later mesovortices were documented by a DOW radar that operated within the eye of Harvey as it passed overland. Individual mesovortices had diameters of 5-8 km with embedded tornado-scale vortices on the order of 1 km in diameter. Analysis of the time series of wind records from *in situ* tower instruments indicated that the gust factors associated with mesovortices reached a value of 2.0, which is considerably higher than the 1.5-1.7 gust factors derived from theoretical turbulence models.

While extreme winds have been observed in mesovortices along the inner eyewall of other hurricanes, this study is the first to present the wind record and gust analysis along with dual-Doppler wind retrievals and detailed radar analysis from ground-based observing systems during landfall of a major hurricane. Additionally, a sounding taken in the eye of Harvey yielded an unprecedented amount of precipitable

15

421 water for atmospheric soundings over the continental United States. Integrated observations of such
422 detail are rather rare within the environment of landfalling hurricanes. Yet, such observations are
423 important to documenting the internal structure of hurricanes and improving plans to mitigate their
424 impact. Moreover, such datasets can be used to validate numerical simulations of hurricane structure at
425 landfall, which would contribute to greater forecast accuracy of extreme impacts at shorter time and space
426 scales.
427
428 While flooding from storm surge remains one of the greatest risk factors during hurricane landfall
429 (Rappaport 2014), inland flooding caused by rainbands, the inner core precipitation, and the eyewall can
430 also lead to a significant number of fatalities in the United States (Rappaport 2000). As the coastal and
431 nearby regions continue to grow in population (Crossett et al. 2004), it will be more difficult to conduct
432 large-area evacuations. While current evacuations are based on storm surge forecasts, as future
433 quantitative surface-wind and precipitation forecasts become more accurate, that information may also
434 assist emergency managers in developing targeted evacuation guidance. Even if a coastal location is not
435 expected to be inundated by surge, the analysis provided here indicates that there remains the threat of
436 extreme winds from mesovortices along the inner edge of the eyewall. It is important to recognize that
437 observation and characterization of the fine scale structures within landfalling tropical cyclones are
438 required to achieve an enhanced level of situational awareness.
439
440 A grand challenge to collecting integrated observations like those documented here is the need to fund
441 programs that collect data *during the event*. In particular, non-federal agency observing platforms have
442 few avenues for obtaining support for such deployments. The variability in the number of landfalling
443 major hurricanes, which may be zero for several consecutive years, gives appropriate pause to reviewers
444 of proposals submitted through the normal grants process. Programs like Rapid Response Research
445 (RAPID), sponsored by the National Science Foundation, tend to focus on collecting data after a disaster
446 instead of during. For instance, the SMART radar team was awarded a RAPID proposal to reimburse their
447 Harvey deployment a few weeks after collecting data during the landfall of Irma.
448
449 Given the short lead times of targets of opportunity, even the special agency programs that are established
450 to fund urgent data collection currently cannot provide timely input for go/no-go deployment decisions in
451 which significant financial resources must be obligated. Consequently, the collection of specialized high
452 temporal and spatial resolution observations needed to further our physical understanding, validate
453 simulated physical processes in numerical models, and improve forecasts and warnings of catastrophic
454 events is severely limited. A paradigm shift in federal agencies' ability to support high-impact, but
455 infrequent, near-zero lead time data collection is required if progress is to be made in addressing the many
456 research questions and their applications described above. Both research and operational agencies should
457 strive to develop appropriate mechanisms to support these operations.
458

459

APPENDIX. Near surface measurements and meta-data from fixed and adaptive mesonets.

Table 1. Metadata for the deployed stations during Hurricane Harvey.

Mesonet	Station Name	Station ID	Landmark	Lat.	Lon.	Height (m)	Avg . Period (min)	Gust Duration (s)
FCMP/Towers	FCMP T2	FCMP T2	Rockport	28.08880	-97.05120	15	1	3
FCMP/Towers	FCMP T3	FCMP T3	Port Lavaca	28.61190	-96.62520	15	1	3
TTU/StickNet	TT0102A	TT0102A	Portland	27.87936	-97.29433	2	1	3
TTU/StickNet	TT0103A	TT0103A	Aransas Pass	27.90926	-97.13204	2	1	3
TTU/StickNet	TT0104A	TT0104A	Rockport	28.11096	-97.02672	2	1	3
TTU/StickNet	TT0105A	TT0105A	Austwell	28.33900	-96.92954	2	1	3
TTU/StickNet	TT0106A	TT0106A	Seadrift	28.43935	-96.72760	2	1	3
TTU/StickNet	TT0108A	TT0108A	Tradewinds	28.03384	-97.23983	2	1	3
TTU/StickNet	TT0110A	TT0110A	Austwell	28.40905	-96.86999	2	1	3
TTU/StickNet	TT0111A	TT0111A	Port Alto	28.66249	-96.41518	2	1	3
TTU/StickNet	TT0112A	TT0112A	Port Lavaca	28.58847	-96.62765	2	1	3
TTU/StickNet	TT0213A	TT0213A	Corpus Christi	27.70409	-97.15087	2	1	3
TTU/StickNet	TT0214A	TT0214A	Corpus Christi	27.58605	-97.21806	2	1	3
TTU/StickNet	TT0220A	TT0220A	Woodsboro	28.16117	-97.20979	2	1	3
CSWR/DOW	DOW8 Ano	DOW8	Rockport	28.08688	-97.04672	8	1	3
CSWR/Pod	PodB	PodB	Rockport	28.08365	-97.04365	1	1	3
CSWR/Pod	PodC	PodC	Rockport	28.08893	-97.04319	1	1	3
CSWR/Pod	PodD	PodD	Rockport	28.11070	-97.02666	1	1	3
NSSL	Mobile Mesonet	Probe 1	Woodsboro	28.04400	-97.33210	3	1	3
NSSL	Mobile Mesonet	Probe 1	Woodsboro	28.22420	-97.34530	3	1	3

466
467
468
469
470
471
472
473
474
475
476
477
478
479

480
481
482
483 **Table 2.** Maximum wind speed data from the deployed stations during Hurricane Harvey.
484

Mesonet	Station ID	Height (m)	Max. Wind (m/s)	Avg . Period (min)	Max. Gust (m/s)	Gust Duration (s)	Captured Peak
FCMP/Towers	FCMP T2	15	49	1	63	3	Yes
FCMP/Towers	FCMP T3	15	23	1	30	3	Yes
TTU/StickNet	TT0102A	2	26	1	34	3	Yes
TTU/StickNet	TT0103A	2	36	1	48	3	Yes
TTU/StickNet	TT0104A	2	35	1	45	3	No
TTU/StickNet	TT0105A	2	37	1	46	3	Yes
TTU/StickNet	TT0106A	2	29	1	39	3	Yes
TTU/StickNet	TT0108A	2	37	1	44	3	Yes
TTU/StickNet	TT0110A	2	35	1	46	3	Yes
TTU/StickNet	TT0111A	2	21	1	27	3	Yes
TTU/StickNet	TT0112A	2	23	1	30	3	Yes
TTU/StickNet	TT0213A	2	34	1	41	3	Yes
TTU/StickNet	TT0214A	2	27	1	35	3	Yes
TTU/StickNet	TT0220A	2	38	1	44	3	No
CSWR/DOW	DOW8	8	46	1	60	3	Yes
CSWR/Pod	PodB	1	25	1	35	3	No
CSWR/Pod	PodC	1	25	1	34	3	No
CSWR/Pod	PodD	1	33	1	44	3	No
NSSL	Probe 1	3	34	1	42	3	Yes
NSSL	Probe 1	3	31	1	39	3	Yes

485
486
487
488
489
490
491
492
493
494
495
496
497
498
499
500
501
502

503
504
505
506 **Table 3.** Metadata for the mesonet stations during Hurricane Harvey.
507

Mesonet	Station Name	Station ID	Lat.	Lon.	Height (m)	Avg. Period (min)	Gust Duration (s)
Earth Networks	Dow Chemical	SDRFT	28.52487	-96.77377	11	2	2
Earth Networks	First Community Bank	CCFCB	27.79630	-97.39213	65	2	2
Earth Networks	KRIS TV	KRIST	27.79237	-97.40117	11	2	2
Earth Networks	Matagorda Bay Pilots	MGBPS	28.43806	-96.41583	12	2	2
Earth Networks	Mike Shaw Kia	CRPMS	27.69750	-97.34777	9	2	2
Earth Networks	Texas Maritime Museum	RCKPR	28.02669	-97.04947	8	2	2
TAMU/TCOON	Aransas Pass Tower	143701	27.83700	-97.03900	14	2	5
TAMU/TCOON	Aransas Wildlife Refuge	AWRT2	28.22773	-96.79658	12	2	5
TAMU/TCOON	Copano Bay	CPNT2	28.11444	-97.02439	9	2	5
TAMU/TCOON	Lavaca Bay	VCAT2	28.64051	-96.60976	6	2	5
TAMU/TCOON	Nueces Bay	NUET2	27.83218	-97.48506	6	2	5
TAMU/TCOON	Packery Channel	PACT2	27.63457	-97.23696	11	2	5
TAMU/TCOON	Port Aransas	RTAT2	27.83975	-97.07270	11	2	5
TAMU/TCOON	Port O'Connor	PCNT2	28.44581	-96.39551	9	2	5
TAMU/TCOON	Seadrift Harbor	SDRT2	28.40730	-96.71220	10	2	5
WeatherFlow	Corpus Christi	XCRP	27.59903	-97.30449	10	1	3
WeatherFlow	Laguna Shores	XLAG	27.63716	-97.28678	10	1	3
WeatherFlow	Matagorda Bay	XMGB	28.59107	-95.98264	6	1	3
WeatherFlow	Wildcat	XWLD	27.86703	-97.32257	5	5	3

508
509
510
511
512
513
514
515
516
517
518
519
520
521
522
523
524
525
526
527

528
529
530
531 **Table 4.** Maximum wind speed data from the mesonet stations during Hurricane Harvey.
532

Mesonet	Station ID	Height (m)	Max. Wind (m/s)	Avg . Period (min)	Max. Gust (m/s)	Gust Duration (s)	Captured Peak
Earth Networks	SDRFT	11	24	2	40	2	No
Earth Networks	CCFCB	65	30	2	45	2	Yes
Earth Networks	KRIST	11	17	2	32	2	Yes
Earth Networks	MGBPS	12	14	2	21	2	No
Earth Networks	CRPMS	9	15	2	24	2	No
Earth Networks	RCKPR	8	21	2	34	2	No
TAMU/TCOON	143701	14	47	2	56	5	Yes
TAMU/TCOON	AWRT2	12	35	2	47	5	Yes
TAMU/TCOON	CPNT2	9	37	2	49	5	Yes
TAMU/TCOON	VCAT2	6	27	2	34	5	Yes
TAMU/TCOON	NUET2	6	26	2	33	5	Yes
TAMU/TCOON	PACT2	11	29	2	37	5	Yes
TAMU/TCOON	RTAT2	11	26	2	35	5	Yes
TAMU/TCOON	PCNT2	9	27	2	35	5	Yes
TAMU/TCOON	SDRT2	10	27	2	37	5	Yes
WeatherFlow	XCRP	10	24	1	34	3	Yes
WeatherFlow	XLAG	10	27	1	36	3	Yes
WeatherFlow	XMGB	6	25	1	29	3	Yes
WeatherFlow	XWLD	5	25	5	33	3	No

533
534
535
536
537
538
539
540
541
542
543
544
545
546
547
548
549
550
551
552

553
554 **Table 5.** Metadata for the state and federal stations during Hurricane Harvey.
555

Network	Station Name	Station ID	Lat.	Lon.	Height (m)	Avg. Period (min)	Gust Duration (s)
FAA/AWOS	Corpus Christi NAS	KNGP	27.68790	-97.29160	10		
FAA/AWOS	Mustang Beach	KRAS	27.80830	-97.08530	10		
FAA/AWOS	Port Lavaca	KPKV	28.64990	-96.67990	10		
NDBC/C-MAN	Port Aransas Pier	PTAT2	27.82591	-97.05064	15	2	3
NOS/OOPS	Bob Hall Pier	MQTT2	27.58102	-97.21650	12	2	5
NOS/OOPS	Matagorda Bay Entrance	138488	28.42200	-96.32700	12	2	5
NOS/OOPS	Rockport	RCPT2	28.01980	-97.04810	7	2	5
NOS/OOPS	South Bird Island - NPS	IRDT2	27.48470	-97.31810	11	2	5
NOS/NERRS	Aransas Pass Channel	MIST2	27.83810	-97.05030	9	15	
NOS/NERRS	Copano East	MAXT2	28.13235	-97.03444	6	15	5
NWS/ASOS	Aransas Airport	KRKP	28.08370	-97.04670	10	2	3
NWS/ASOS	Corpus Christi Intl	KCRP	27.77340	-97.51300	10	2	3
USFS/RAWS	Aransas NWR	AFWT2	28.30444	-96.82333	6	10	5
USFS/RAWS	Matagorda Island	MIRT2	28.12278	-96.80222	6	10	5

556
557
558
559 **Table 6.** Maximum wind speed data from the state and federal stations during Hurricane Harvey.
560

Network	Station ID	Height (m)	Max. Wind (m/s)	Avg. Period (min)	Max. Gust (m/s)	Gust Duration (s)	Captured Peak
FAA/AWOS	KNGP	10	28		33		No
FAA/AWOS	KRAS	10	24		30		No
FAA/AWOS	KPKV	10	17		22		No
NDBC/C-MAN	PTAT2	15	43	2	56	3	Yes
NOS/OOPS	MQTT2	12	25	2	33	5	Yes
NOS/OOPS	138488	12	28	2	34	5	Yes
NOS/OOPS	RCPT2	7	30	2	48	5	No
NOS/OOPS	IRDT2	11	24	2	32	5	Yes
NOS/NERRS	MIST2	9	43	15	0		No
NOS/NERRS	MAXT2	6	37	15	52	5	No
NWS/ASOS	KRKP	10	23	2	31	3	No
NWS/ASOS	KCRP	10	22	2	28	3	No
USFS/RAWS	AFWT2	6	23	10	48	5	Yes
USFS/RAWS	MIRT2	6	23	10	37	5	No

561
562
563
564
565

566
567 **Table 7.** Maximum wind speed data from aircraft reconnaissance mission SFMR and Dropsonde
568 observations during Hurricane Harvey.
569

Station Name	Station ID Measurement	Lat.	Lon.	Height (ft)	Gust (mph)	Effective Duration (s)
Mission 19 / Ob 17	KNHC-Dropsonde	27.65000	-96.53000	10	61	10
Mission 19 / Ob 35	KNHC-Dropsonde	27.90000	-96.75000	10	58	10
Mission 20 / Ob 04	KNHC-Dropsonde	28.02000	-96.90000	10	62	10
Mission 20 / Ob 06	KNHC-Dropsonde	27.80000	-96.90000	10	52	10
Mission 20 / Ob 15	KNHC-Dropsonde	27.96000	-96.94000	10	57	10
Mission 19 / Ob 29	KNHC-SFMR	27.66700	-96.71700	10	58	10
Mission 19 / Ob 42	KNHC-SFMR	27.86700	-96.56700	10	54	10
Mission 20 / Ob 13	KNHC-SFMR	28.05000	-96.71700	10	55	10
Mission 20 / Ob 14	KNHC-SFMR	27.76700	-96.91700	10	54	10
Mission 20 / Ob 18	KNHC-SFMR	27.83300	-96.96700	10	55	10
Mission 20 / Ob 18	KNHC-SFMR	27.93300	-97.05000	10	53	10
Mission 20 / Ob 19	KNHC-SFMR	28.08300	-96.73300	10	56	10
Mission 20 / Ob 25	KNHC-SFMR	28.15000	-96.71700	10	55	10

570
571
572
573
574
575
576
577
578
579
580
581
582
583
584
585
586
587
588
589
590
591
592
593
594
595
596
597
598

REFERENCES

Abdullah, A. J., 1966: The Spiral Bands of a Hurricane: A Possible Dynamic Explanation. *J. Atmos. Sci.*, **23**, 367–375.

Aberson, S. D., M. T. Montgomery, M. M. Bell, and M. Black, 2006: Hurricane Isabel (2003); New insights into the physics of intense storms. Part II: Extreme localized wind. *Bull. Am. Meteorol. Soc.*, **87**, 1349–1354, doi:10.1175/BAMS-87-10-1349.

Aberson, S. D., J. A. Zhang, K. Nuñez Ocasio, S. D. Aberson, J. A. Zhang, and K. N. Ocasio, 2017: An extreme event in the eyewall of Hurricane Felix on 2 September 2007. *Mon. Weather Rev.*, MWR-D-16-0364.1, doi:10.1175/MWR-D-16-0364.1.

Alford, A. A., and M. I. Biggerstaff, 2015: High-resolution dual-Doppler observations of tropical cyclone vortex Rossby waves. Preprints, 37th Intern. Conf. on Radar Meteor., Amer. Meteor. Soc., available at https://ams.confex.com/ams/37RADAR/webprogram/Paper275848.html.

Alford, A. A., and M. I. Biggerstaff, 2017: Mobile radar observations of the kinematics and microphysics of Hurricanes Isaac (2012) and Hermine (2016). Preprints, 38th Intern. Conf. on Radar Meteor., Amer. Meteor. Soc., available at https://ams.confex.com/ams/38RADAR/meetingapp.cgi/Paper/320753.

Alford, A. A., M. I. Biggerstaff, and D. P. Betten, 2016: Mobile radar observation of vortex Rossby waves in three landfalling tropical cyclones. Preprints, 32nd Conf. on Hurricanes and Tropical Meteor., Amer. Meteor. Soc., available at https://ams.confex.com/ams/32Hurr/webprogram/Paper293013.html.

Avallone, L.M. and B. Baeuerle, 2017: A 20-year history of NSF-supported atmospheric science field campaigns. Bull. Amer. Meteor. Soc., 1333-1339, DOI:10.1175/BAMS-D-15-00222.1.

Baker, A. K., M. D. Parker, and M. D. Eastin, 2008: Environmental ingredients for supercells and tornadoes within Hurricane Ivan. Weather and Forecasting, 24, 223-224, doi: 10.1175/2008WAF2222146.1.

Balderrama, J.A., F.J. Masters, K.R. Gurley, D.O. Prevatt, L.D. Aponte-Bermudez, T.A. Reinhold, J.-P. Pinelli, C.S. Subramanian, S.D. Schiff, and A.G. Chowdhury, 2011: The Florida Coastal Monitoring Program (FCMP): A review. J. Wind Eng. Ind. Aerodyn., 99(9), 979-995.

Biggerstaff, M. I., L. J. Wicker, J. Guynes, C. Ziegler, J. M. Straka, E.N. Rasmussen, A. Dogget IV, L. D. Carey, J. L. Schroeder, and C. Weiss, 2005: The Shared Mobile Atmospheric Research and Teaching (SMART) Radar: A collaboration to enhance research and teaching. *Bull. Amer. Meteor. Soc.*, **86**, 1263-1274, doi: 10.1175/BAMS-86-9-1263.

Biggerstaff, M. I., Z. Zounes, A. A. Addison, G. D. Carrie, J. T. Pilkey, M. A. Uman, and D. M. Jordan, 2017: Flash propagation and inferred charge structure relative to radar-observed ice alignment signatures in a small Florida Mesoscale Convective System, *Geophys. Res. Lett.,* **44***, 8027-8036, doi:10.1002/2017GL074610.*

Black, P. G. and F. D. Marks, 1991: The structure of an eyewall mesovortex in hurricane Hugo. *Proc. 19th Conf. on Hurr. and Trop. and Meteor.*, Miami, FL., Amer. Meteor. Soc., 579-582.

648   Black, P. G., S. J. Buchan, and R. L. Cohen, 1999: The tropical cyclone eyewall mesovortex: A physical
649   mechanism explaining extreme peak gust occurrence in TC Olivia, 4 April 1996 on Barrow Island,
650   Australia. *Proc. 31st Offshore Technology Conf.*, Houston, TX, 3-6 May 1999, OTC 10792.

651

652   Braun, S. A., 2002: A Cloud-Resolving Simulation of Hurricane Bob (1991): Storm Structure and
653   Eyewall Buoyancy. *Mon. Weather Rev.*, **130**, 1573–1592, doi:10.1175/1520-
654   0493(2002)130<1573:ACRSOH>2.0.CO;2.

655

656   Chen, Y., and M. K. Yau, 2001: Spiral Bands in a Simulated Hurricane. Part I: Vortex Rossby Wave
657   Verification. *J. Atmos. Sci.*, **58**, 2128–2145, doi:10.1175/1520-0469(2001)058<2128:SBIASH>2.0.CO;2.

658

659   Corbosiero, K. L., J. Molinari, A. R. Aiyyer, and M. L. Black, 2006: The Structure and Evolution of
660   Hurricane Elena (1985). Part II: Convective Asymmetries and Evidence for Vortex Rossby Waves. *Mon.*
661   *Weather Rev.*, **134**, 3073–3091, doi:10.1175/MWR3250.1.

662

663   Crossett, K. , T. J. Culliton , P. Wiley , and T. R. Goodspeed, 2004: Population Trends along the Coastal
664   United States, 1980–2008. Silver Spring, Maryland. National Oceanic and Atmospheric Administration,
665   47 p.

666

667   Curtis, Lon, 2003: Midlevel dry intrusions as a factor in tornado outbreaks associated with landfalling
668   tropical cyclones from the Atlantic and Gulf of Mexico. *Weather and Forecasting*, **19**, 411-427.

669

670   Eastin, M. D., W. M. Gray, and P. G. Black, 2005: Buoyancy of Convective Vertical Motions in the Inner
671   Core of Intense Hurricanes. Part II: Case Studies. *Mon. Weather Rev.*, **133**, 209–227, doi:10.1175/MWR-
672   2849.1. http://journals.ametsoc.org/doi/abs/10.1175/MWR-2849.1.

673

674   Fernández-Cabán, P.L. and F.J. Masters, 2017: Near surface wind longitudinal velocity positively skews
675   with increasing aerodynamic roughness length. J. Wind Eng. Ind. Aerodyn., 169, 94-105.

676

677   Fernández-Cabán, P.L., B.M. Phillips, F.J. Masters, [author list of contributors to curated data], 2017:
678   [title], DesignSafe-CI [publisher], Dataset, https://doi.org/[placeholder].

679

680   Gao, C., and P. Zhu, 2016: Vortex Rossby wave propagation in baroclinic tropical cyclone-like vortices.
681   *Geophys. Res. Lett.*, **43**, 578-589, doi:10.1002/2016GL071662.

682

683   Gentry, R. C., 1983: Genesis of tornadoes associated with hurricanes. *Mon. Wea. Rev.* **111,** 1793–1805.

684

685   Hirth, Brian D., J. L. Schroeder, C. C. Weiss, D. A. Smith, and M. I. Biggerstaff, 2012: Research radar
686   analysis of the internal boundary layer over Cape Canaveral, FL during the landfall of Hurricane Frances
687   (2004), *Wea. Forecasting,* **27***,* 1349-1372, doi:10.1175/WAF-D-12-00014.1.

688

689   Ho, F. P. and J. F. Miller, 1982: Pertinent Meteorological and Hurricane Tide Data for Hurricane Carla -
690   August 1982, NOAA Tech Report NWS 32, PB83 118240.

691

692   Knupp, K. R., J. Walters, and M. Biggerstaff, 2006: Doppler profiler and radar observations of boundary
693   layer variability during the landfall of Tropical Storm Gabrielle. *J. Atmo. Sci.,* **63,** 234-251, doi:
694   10.1175/JAS3608.1.

695

696   Kosiba, K., J. Wurman, F.J. Masters, P. Robinson and C. Alexander, 2013: Mapping of near-surface
697   winds in Hurricane Rita using fine-scale radar, anemometer, and land-use data. Monthly Weather Review,
698   141, 4337–4349.
699

700   Kwon, D-K and A. Kareem, 2009: Gust-front factor: new framework for wind load effects on structures.
701   *J. Struct. Eng.*, **135**(6), 717-732.
702

703   Lorsolo, S., J. L. Schroeder, P. Dodge, and F. Marks, Jr., 2008: An observational study of hurricane
704   boundary layer small-scale coherent structures. *Mon. Wea. Rev.*, **136**, 2871-2893.
705

706   Marks, F.D., Jr., and Coauthors, 1998. Landfalling Tropical Cyclones: Forecast Problems and Associated
707   Research Opportunities. *Bull. Amer. Meteor. Soc.* **79,** 305-323.
708

709   Marks, F. D., P. G. Black, M. T. Montgomery, and R. W. Burpee 2008: Structure of the eye and eyewall
710   of   Hurricane   Hugo   (1989).   Mon.   Wea.   Rev.,   136,   1237-1259.
711   doi:http://dx.doi.org/10.1175/2007MWR2073.1
712

713   Masters, F.J., P.J. Vickery, P. Bacon, and E.N. Rappaport, 2010: Toward objective, standardized intensity
714   estimates from surface wind speed observations. Bull. Amer. Meteor. Soc., 91, 1665-1682.
715

716   McCaul, E. W., Jr., Jr., 1987: Observations of the Hurricane ''Danny'' tornado outbreak of 16 August
717   1985. *Mon. Wea. Rev.,* **115,** 1206–1223.
718

719   McCaul, E. W., Jr., and M. L. Weisman (1996): "Simulations of shallow supercell storms in landfalling
720   hurricane environments." *Mon. Wea. Rev.*, **124**, 408-429.
721

722   Menelaou, K., and M. K. Yau, 2014: On the role of asymmetric convective bursts to the problem of
723   hurricane intensification. Radiation of vortex Rossby waves and wave-mean flow interactions. *J. Atmos.*
724   *Sci.*, 140212115924008, doi:10.1175/JAS-D-13-0343.1.
725

726   McCaul Jr., Eugene W., 1991: Buoyancy and shear characteristics of hurricane-tornado environments.
727   *Mon. Wea. Rev.*, **119**, 1954-1978.
728

729   Montgomery, M. T., and R. J. Kallenbach, 1997: A theory for vortex Rossby-waves and its application to
730   spiral bands and intensity changes in hurricanes. *Quart. J. Roy. Meteor. Soc.*, **123**, 435–465,
731   doi:10.1002/qj.49712353810.
732

733   NOAA NWS, 2017: Post-tropical cyclone report, Harvey. Accessed 13 November 2017,
734   https://nwschat.weather.gov/p.php?pid=201711131514-KHGX-ACUS74-PSHHGX.
735

736   Persing, J., and M. T. Montgomery, 2003: Hurricane Superintensity. *J. Atmos. Sci.*, **60**, 2349–2371,
737   doi:https://doi.org/10.1175/1520-0469(2003)060%3C2349:HS%3E2.0.CO;2.
738

739   Pilkey, J., M. A. Uman, J. D. Hill, T. Ngin, W. Gamerota, D. Jordan, W. Rison, P. Krehbiel, H. Edens, M.
740   I. Biggerstaff, and P. Hyland, 2013: Rocket-and-wire triggered lightning in 2012 Tropical Storm Debby
741   in the absence of natural lightning. *J. Geophys. Res. Atmos.,118, 13158-13174*
742

743   Rappaport, E. N., 2000: Loss of life in the United States associated with recent Atlantic tropical cyclones.
744   *Bull. Amer. Meteor. Soc.*, **81**, 2065-2073.

745

746 Rappaport, E. N., 2014: Fatalities in the United States from Atlantic Tropical Cyclones: New Data and
747 Interpretation. *Bull. Am. Meteorol. Soc.*, **95**, 341–346, doi:10.1175/BAMS-D-12-00074.1.
748 http://journals.ametsoc.org/doi/abs/10.1175/BAMS-D-12-00074.1.

749

750 Rathje, E.M., C. Dawson, J.E. Padgett, J.P. Pinelli, D. Stanzione, A. Adair, P. Arduino, S.J. Brandenberg,
751 T. Cockerill, C. Dey, M. Esteva, F.L. Haan, Jr., M. Hanlon, A. Kareem, L. Lowes, S. Mock, and G.
752 Mosqueda, 2017: DesignSafe: A new cyberinfrastructure for natural hazards engineering. ASCE Natural
753 Hazards Review, **18**, 3, https://doi.org/10.1061/(ASCE)NH.1527-6996.0000246.

754

755 Rogers, J. W., R. L. Thompson, and P. T. Marsh, 2014: Potential applications of a CONUS sounding
756 climatology developed at the Storm Prediction Center. *27th Conf. Severe Local Storms*, Madison, WS,
757 Amer. Meteor. Soc., 145, https://ams.confex.com/ams/27SLS/webprogram/Paper255385.html.

758

759 Rogers, R., S. Aberson, M. Black, P. Black, J. Cione, P. Dodge, J. Dunion, J. Gamache, J. Kaplan, M.
760 Powell, and others. 2006. The Intensity Forecasting Experiment: A NOAA multiyear field program for
761 improving tropical cyclone intensity forecasts. *Bull. Amer. Meteor. Soc.* **87**, 1,523–1,537.

762

763 Spratt, S., Sharp., Welsh, P., Sandrik., Alsheimer, F., Paxton, C., 1997: A WSR-88D Assessment of
764 Tropical Cyclone Outer Rainband Tornadoes. *Wea. Forecasting,* **12**, 479-510.

765

766 Verbout, S. M., D. M. Schultz, L. M. Leslie, H. E. Brooks, D. J. Karoly, and K. L. Elmore, 2007: Tornado
767 outbreaks associated with landfalling hurricanes in the north Atlantic Basin: 1954–2004. *Meteorol Atmos*
768 *Phys*, **97**, 255–271.https://doi.org/10.1007/s00703-006-0256-x

769

770

771 Von Karman, T., 1948. Progress in the statistical theory of turbulence. *Proceedings of the National*
772 *Academy of Sciences*, *34*(11), pp.530-539.

773

774 Weiss, C. C., and J. L. Schroeder, 2008: "StickNet: A New Portable Rapidly Deployable Surface
775 Observation System," *Bulletin of the American Meteorological Society*, **89**, 1502-1503.

776

777 Willoughby, H. E., 1984: Stationary and Moving Convective Bands in Hurricanes. *J. Atmos. Sci.,* **41**.,
778 3189-3211.

779

780 Wingo, S. M. and K. R. Knupp, 2016: Kinematic structure of mesovortices in the eyewall of hurricane Ike
781 (2008) derived from ground-based dual-Doppler analyses. *Mon. Wea. Rev.*, **144**, 4245-4263.

782

783 Wurman, J. and K. Kosiba, 2017: The Role of Small-Scale Vortices in Enhancing Surface Winds and
784 Damage in Hurricane Harvey, *Mon. Weather Rev*, https://doi.org/10.1175/MWR-D-17-0327.1

785

786 Wurman, J., and J. Winslow, 1998: Intense sub-kilometer boundary layer rolls in Hurricane Fran, *Science*,
787 **280**, 555–557.

788

26